

Andreev reflection in nodal-line Weyl semimetal

Chunxu Bai[✉] and Yanling Yang

College of Physics and Electronic Engineering, Xinyang Normal University, Xinyang, 464000, People's Republic of China

E-mail: chunxu_bai@163.com

Received 21 November 2019, revised 8 January 2020

Accepted for publication 27 January 2020

Published 6 February 2020



Abstract

Based on the Bogoliubov-de Gennes equation, the quantum scattering problem through a nodal-line Weyl semimetal based normal metal/superconductor heterojunction has been theoretically studied. Since the crystallographic anisotropy in the material, two different orientations between the crystalline axis and the superconducting interface have been revealed. Considering a heterojunction with the interface paralleling to the basal plane, it is found that Andreev reflection with $k_{\parallel} = \sqrt{m/B}$ due to Klein-like scattering gives rise to a perfect scattering. Deviation from the critical value, Andreev reflection falls down and normal reflection goes up. While the interface is perpendicular to the basal plane, the pure intra-mode retro-Andreev reflection (RAR) and inter-mode specular Andreev reflection (SAR) are manifested at the normal incident. Moreover, the reflection coefficient exhibits the reentrant behavior with the Fermi energy. Fundamentally, such features are a consequence of the torus-like iso-energy surfaces of the nodal-line Weyl semimetals, which is in sharp contrast to the case of conventional materials, graphene, and Weyl-point semimetals. Those novel scattering processes also result in a distinctive tunneling conductance, such as the sub-gap nonmonotonic features, the interface directional dependent zero bias conductances and the reentrant behavior, which can be served as a smoking gun to distinguish the mode-resolved Andreev reflections in experiments.

Keywords: Andreev reflection, nodal-line Weyl semimetal, inter-and intra-mode scattering

(Some figures may appear in colour only in the online journal)

1. Introduction

Topological materials, from the two dimensional quantum spin hall material to three dimensional topological insulator and three dimensional Weyl semimetal, have aroused great interest in recent years [1–7]. Interestingly, different from the topological insulator, the topological surface Fermi arc and the bulk chiral anomaly effect make the Weyl semimetal a star material to expand the potentiality of the novel topological state. Weyl semimetal was first theoretically predicted by Wan *et al* in a class of pyrochlore iridates (such as $\text{Y}_2\text{Ir}_2\text{O}_7$) in the year 2011 [8]. To get rid of the magnetic material, another kind of the lattice inversion symmetry broken material has been independently reported by two groups in 2015 [9, 10]. Following that, a lot of Weyl semimetal materials have been

revealed by the angle-resolved photoemission spectroscopy, such as, TaAs [11, 12], TaP [13, 14], NbAs [15], MoTe_2 [16, 17], and $\text{Mo}_x\text{W}_{1-x}\text{Te}_2$ [18, 19]. Very recently, the Weyl point as well as the exotic Fermi arc has also been confirmed both by experimental measurement and theoretical calculation in the magnetic material YbMnBi_2 [20]. Moreover, although the spinful topological nodal line has been proposed by the first-principles calculation in HgCr_2Se_4 [21] and TiTaSe_2 [22], the detailed angle-resolved photoemission spectroscopy measurement shows that the Weyl nodal line which surrounds the Γ point can be realized in a single layer GdAg_2 [23]. Those experimental results suggest that the Weyl semimetal can be made implemented in specific materials. Based on the crossing of the conduction and the valence band in the Brillouin zone, three dimensional Weyl semimetals can be

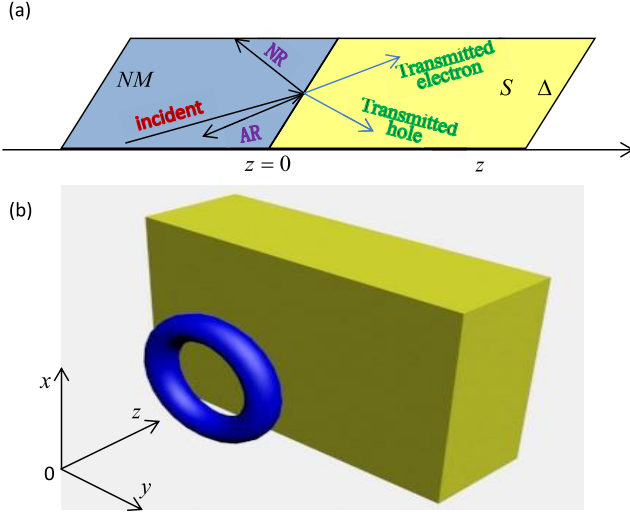


Figure 1. Interface parallel to the basal plane. Panel (a): schematic diagram of scattering processes in the nodal-line Weyl semimetal based NM/S heterojunction. Incident, reflected (NR and AR), and transmitted waves near the interface are shown schematically by the lines with arrows. Superconducting gap potential in S lead is given as Δ . (b) Relative orientations of the interface and the iso-energy surface of the NM lead. The iso-energy surface is defined by $(\mu + \varepsilon)^2 = (m - Bk_{//})^2 + (k_N^e)^2$. It is shown by torus in the reciprocal space. The S lead is shown as a yellow parallelepiped. Thus the basal plane (the $x - y$ plane) in the NM lead parallels to the NM/S interface.

into the Weyl-point semimetal and the nodal-line Weyl semimetal [7, 24]. In the former case, there are type-I Weyl semimetal and type-II Weyl semimetal in which low energy band shows linear characteristic in three-dimensional Brillouin zone through a node termed a Weyl point. In the latter case, the energy band crossing across the Brillouin zone winds into a closed loop called a nodal line. Note that we term the plane of the closed nodal line as the basal plane, as shown (the $x - y$ plane) in figures 1 and 2. In the reciprocal space, the energies of the quasiparticles exhibit a distinctive anisotropy and hold a torus-like isoenergy surface.

Although lots of angle-resolved photoemission spectroscopy experiments have been launched in the past years, the transport properties also play a key role in understanding and applying the topological Weyl semimetals. Therefore, the special property has induced a series of intriguing features from both fundamental research and electronic applications aspect [25–34]. In this respect, there have been a number of studies which focus on the three dimensional Klein tunneling in the topological Weyl semimetals addressed, such as, Klein tunneling and magnetoresistance in p-n junctions [25], Klein tunneling of Weyl fermions through a barrier potential with and without the influence of magnetic fields [26, 27], and chiral tunneling in the electrostatic potential gates [28–30]. Moreover, fundamental phenomena and promising applications in the Weyl semimetal based superconducting heterojunction have also been revealed, such as the specular Andreev reflection (SAR) and the chirality blockade of Andreev reflection (AR) in type-I Weyl semimetal [31, 32], and most recently, the double ARs in type-II Weyl semimetal [31, 32].

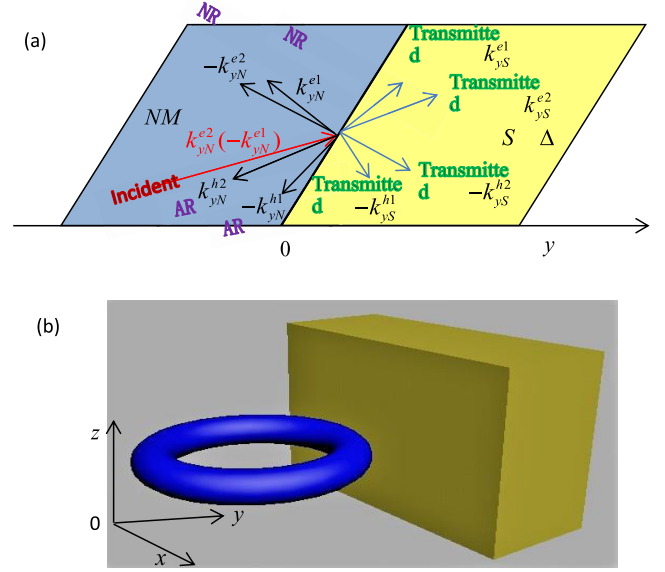


Figure 2. Interface perpendicular to the basal plane. Panel (a): Schematic diagram of scattering processes in the present NM/S heterojunction. Incident, reflected (AR and NR), and transmitted waves near the interface are shown schematically by the lines with arrows. Superconducting gap potential in S lead is given as Δ . (b) Relative orientations of the interface and the iso-energy surface of the NM lead. It is shown that the basal plane (the $x - y$ plane) of the torus-like iso-energy surface in NM lead is perpendicular to the NM/S interface. We fix y axis to be normal to the interface.

In general, AR process denotes that an incident electron-like quasiparticle is reflected back as a hole-like quasiparticle at the superconducting interface, and a Cooper pair jumps into the superconductor [35]. If the reflected hole-like quasiparticle comes back with a same angle of the incident angle, we term it as retro-Andreev reflection (RAR). In fact, the SAR has been predicted in several setups, such as graphene based superconducting heterojunction with and without the spin orbit interaction and the conventional superconducting heterojunction [36–41]. Nonetheless, due to the charge carrier scattering and the strong potential fluctuations in graphene and the negligible signal value in conventional semiconductor, it is an extremely difficult work to experimentally detect the SAR in graphene and in conventional semiconductor [41, 42]. Recently, a hallmark for the transition between the usual RAR and the special SAR has been found in an unprecedentedly clean bilayer graphene-based superconducting heterojunction [43].

In general, the energy band structure near the Fermi energy plays a key role on its transport properties of a material. Therefore, we expect that the nodal-line Weyl semimetal with exotic energy band structure should provide a great opportunity to reveal novel scattering features and detect the SAR. This work is devoted to revealing those issues. Indeed, for the superconducting interface parallel to the basal plane, it is found that AR is perfect at $k_{//} = \sqrt{m/B}$ due to Klein-like scattering. Deviating from the critical value, AR is suppressed and normal reflection (NR) is enhanced. In contrast to graphene, conventional semiconductor material, and Weyl-point semimetal, there is an allowed angle interval around the limit

value $k_{//} = \sqrt{m/B}$. Beyond that, all incident electron-like quasiparticles are reflected back completely. While for the case of the superconducting interface perpendicular to the basal plane, only one kind of the intra-mode RAR and the inter-mode SAR is manifested at the normal incident. This is dissimilar to the case of graphene and Weyl-point semimetal, where the ARs are perfect [33, 34, 36]. Different from the small incident mode, the scattering coefficients exhibit non-monotonic behavior as a function of the Fermi energy. In particular, they exist a perfect intra-mode RAR and a chirality blockade of the intra-mode RAR [32]. For the oblique incidence, an incident forbidden zone can be clearly seen from the both modes. Note that the chirality blockade of the intra-mode RAR has been destroyed by the nonzero z component of the incident mode. The existence of those novel scattering features can be elucidated by the complicated torus-like iso-energy surface of the nodal-line semimetal. Moreover, the characteristic features of the reflection coefficients can be manifested in the corresponding tunneling conductances, so it would offer the experimental measurable signals to diagnose those novel scattering processes.

The rest of this paper is organized as follows. In the next section, the model structures, the calculation methods and the analytical derivative results of the scattering processes in limit cases are introduced. The numerical results of the novel intra-mode RAR and inter-mode SAR scattering processes in the typical nodal-line Weyl semimetal based NM/S superconducting heterojunction are discussed in section 3. In section 4, we give a short summary.

2. Theory and model

2.1. Interface parallel to basal plane

First a typical nodal-line Weyl semimetal based NM/S superconducting heterojunction with the interface paralleling to the basal plane is assumed, as shown in figure 1. The growth direction is taken along the z axis. The NM and the S occupy $z < 0$ and $z > 0$, respectively. The superconducting potential is assumed as a s -wave pairing and taken in the form $\Delta(z) = \Delta\Theta(z)$, where $\Theta(z)$ is the Heaviside step function [36–41]. Since the electrical potential can be modulated independently by the gate voltage or doping, we also set the potential through the NM/S superconducting heterojunction as $U(z) = \begin{cases} 0, & z \leq 0, \\ V_S, & z \geq 0. \end{cases}$ [36]. Since we assume that the transversal width (in the x and y directions) extends to a big enough value and the interface is a perfect flat, thus the momentum components k_x and k_y are conserved in the quantum scattering processes.

In a single particle picture, overlooking the disorder and impurity, we employ the following Bogoliubov-de Gennes equation to describe the quantum scattering processes through the present NM/S superconducting heterojunction [36–41].

$$\begin{pmatrix} H_0 - \mu & \Delta(z) \\ \Delta^*(z) & \mu - H_0 \end{pmatrix} \Psi = \varepsilon \Psi \quad (1)$$

where $H_0(\vec{k}) = (m - Bk_{//}^2)\sigma_x + k_z\sigma_z + U(z)\tau_z$, the four-components spinor $\Psi = (u_{\vec{k}\uparrow}, u_{\vec{k}\downarrow}, v_{-\vec{k}\downarrow}, v_{-\vec{k}\uparrow})^T$ contains the electron-like quasiparticles $((u_{\vec{k}\uparrow}, u_{\vec{k}\downarrow})^T)$ and the hole-like quasiparticles $((v_{-\vec{k}\downarrow}, v_{-\vec{k}\uparrow})^T)$, ε is the excitation energy with respect to μ , $\sigma_{x,z}$ are the Pauli matrices, $\vec{k} = (k_x, k_y, k_z)$ is the three dimension single-particle momentum, $k_{//}^2 = k_x^2 + k_y^2$ is parallel component of momentum, m can be regarded as the rest mass, and $1/(2B)$ can be analogous to an inertial mass in the $x - y$ plane.

In NM lead (where $\Delta = 0$ and $U = 0$), overlooking the parallel momentum component $k_{//}$, the wavefunctions can be expressed in general form as

$$\begin{aligned} \Psi_N^{e\pm}(z) &= \begin{pmatrix} 1 & \frac{\varepsilon + \mu \mp k_{zN}^e}{m - Bk_{//}^2} & 0 & 0 \end{pmatrix} e^{\pm i k_{zN}^e z} \\ \Psi_N^{h\pm}(z) &= \begin{pmatrix} 0 & 0 & 1 & \frac{\mu - \varepsilon \mp k_{zN}^h}{m - Bk_{//}^2} \end{pmatrix} e^{\pm i k_{zN}^h z} \end{aligned} \quad (2)$$

where $k_{zN}^e = \sqrt{(\mu + \varepsilon)^2 - (m - Bk_{//}^2)^2}$ and $k_{zN}^h = \sqrt{(\mu - \varepsilon)^2 - (m - Bk_{//}^2)^2}$ are the z direction momentums of the electron-like quasiparticles and the hole-like quasiparticles, respectively. Note that, to describe a quasiparticle impinging freely on the NM/S interface, the electron-like quasiparticles' wavefunctions must have purely real k_{zN}^e , i.e. $(m - \mu - \varepsilon)/B < (k_{zN}^e)^2 < (m + \mu + \varepsilon)/B$.

Similarly, the spinor wavefunctions in S can be given by

$$\begin{aligned} \Psi_S^{e\pm}(z) &= \begin{pmatrix} 1 & w_e^\pm & \Gamma_e & -\frac{m - Bk_{//}^2 \mp w_e^\pm (k_{zS}^e \mp (V_S - \varepsilon - \mu))}{\Delta} \end{pmatrix} e^{\pm i k_{zS}^e z} \\ \Psi_S^{h\pm}(z) &= \begin{pmatrix} 1 & w_h^\pm & \Gamma_h & -\frac{m - Bk_{//}^2 \mp w_h^\pm (k_{zS}^h \mp (V_S - \varepsilon - \mu))}{\Delta} \end{pmatrix} e^{\pm i k_{zS}^h z} \end{aligned} \quad (3)$$

where $k_{zS}^e = \sqrt{(V_S - \mu)^2 - (m - Bk_{//}^2)^2 - \Delta^2 + \varepsilon^2 + 2\sqrt{(\varepsilon^2 - \Delta^2)(V_S - \mu)^2}}$ and $k_{zS}^h = \sqrt{(V_S - \mu)^2 - (m - Bk_{//}^2)^2 - \Delta^2 + \varepsilon^2 - 2\sqrt{(\varepsilon^2 - \Delta^2)(V_S - \mu)^2}}$ are the z direction momentums of the electron-like quasiparticles and the hole-like quasiparticles in S . The factors in the wavefunctions are given as, $w_e^\pm = \frac{(m - Bk_{//}^2)^2 + \Delta^2 - \varepsilon^2 + (k_{zN}^e \pm (V_S + \mu))^2}{2(Bk_{//}^2 - m)(V_S - \mu)}$, $\Gamma_e = \frac{\varepsilon(V_S - \mu) + \sqrt{(\varepsilon^2 - \Delta^2)(V_S - \mu)^2}}{\Delta(V_S - \mu)}$, $w_h^\pm = \frac{(m - Bk_{//}^2)^2 + \Delta^2 - \varepsilon^2 + (k_{zN}^h \pm (V_S + \mu))^2}{2(Bk_{//}^2 - m)(V_S - \mu)}$, and $\Gamma_h = \frac{\varepsilon(V_S - \mu) - \sqrt{(\varepsilon^2 - \Delta^2)(V_S - \mu)^2}}{\Delta(V_S - \mu)}$. Since the momentum components k_{xN} and k_{yN} are conserved, the factor $e^{ik_{xN}x + ik_{yN}y}$ in the wavefunctions in NM lead and S lead is omitted for brevity.

To solve the scattering properties in the nodal-line Weyl semimetal based NM/S (shown as figure 1), we suppose an electron-like quasiparticle with energy ε is incident from the left NM lead. Thus the wavefunctions in the present heterojunction are

$$\begin{cases} \Psi_N = \Psi_{zN}^{e+} + r\Psi_{zN}^{e-} + r_A\Psi_{zN}^{h+}, & z < 0 \\ \Psi_S = t_e\Psi_{zS}^{e+} + t_h\Psi_{zS}^{h-}, & z > 0 \end{cases} \quad (4)$$

where r and r_A are the amplitudes of normal reflection (NR) and AR in NM lead, respectively, and t_e and t_h are the transmission amplitudes of the electron-like quasiparticle and hole-like quasiparticle in S lead. Note that, the evanescent wave

functions of the AR hole in *NM* lead should be taken into account to guarantee the conservation of probabilistic current.

To obtain the amplitudes in equation (4), we match the wavefunctions in *NM* lead and *S* lead at the interface by the continuity boundary condition $\Psi_N(0) = \Psi_S(0)$. By solving the boundary condition, the expression for r and r_A can be obtained.

Based on the reflection amplitudes and the Blonder–Tinkham–Klapwijk theory, the zero temperature differential conductance of the nodal-line Weyl semimetal based *NM/S* can be given by the following formula [36–41, 44],

$$G(\varepsilon) = G_0 \int (1 - |r|^2 + |r_A|^2) dk_{//} \quad (5)$$

where $G_0 = e^2 S / (\hbar (2\pi)^3)$ is the ballistic conductance of metallic nodal-line Weyl semimetal, S is the area of the junction in the $x - y$ plane. Combining equations (4) and (5), the zero temperature tunneling conductances in the nodal-line Weyl semimetal based *NM/S* can be investigated extensively and easily by the numerical calculations.

2.2. Interface perpendicular to basal plane

Next a nodal-line Weyl semimetal based *NM/S* superconducting heterojunction with the interface perpendicular to the basal plane is assumed, as shown in figure 2. The growth direction is taken along the y axis. The *NM* and the *S* occupy $y < 0$ and $y > 0$, respectively. A s -wave pairing superconducting potential is assumed and given as $\Delta(y) = \Delta\Theta(y)$ [36–41]. The electrical potential energy through the *NM/S* superconducting heterojunction is set as $U(y) = \begin{cases} 0, & y \leq 0, \\ V_S, & y \geq 0. \end{cases}$ [36].

Since we assume that the transversal width is (in the x and z directions) big enough and the interface is ideally flat, the momentum components k_x and k_z are conserved in the present quantum scattering processes.

Similar to the above part A, the wavefunctions in the present heterojunction can also be given by solving the equation. Similar to the equation (1). In *NM* lead (where $\Delta = 0$ and $U = 0$), overlooking the conserved momentum k_{xN} and k_{zN} , the wavefunctions can be expressed in general form as

$$\begin{aligned} \Psi_{N1(2)}^{e\pm}(y) &= \begin{pmatrix} 1 & \frac{m - Bk_{//}^2}{k_{yN}^{e1(2)} - V_S + \varepsilon + \mu} & 0 & 0 \end{pmatrix} e^{\pm i k_{yN}^{e1(2)} y} \\ \Psi_{N1(2)}^{h\pm}(y) &= \begin{pmatrix} 0 & 0 & 1 & \frac{m - Bk_{//}^2}{k_{yN}^{h1(2)} - V_S - \varepsilon + \mu} \end{pmatrix} e^{\pm i k_{yN}^{h1(2)} y} \end{aligned} \quad (6)$$

where $k_{yN}^{e1(2)} = \sqrt{\frac{1}{B} (m - Bk_{xN}^2 - (+)\sqrt{(\mu + \varepsilon - V_S)^2 - k_{zN}^2})}$ and $k_{yN}^{h1(2)} = \sqrt{\frac{1}{B} (m - Bk_{xN}^2 - (+)\sqrt{(\mu - \varepsilon - V_S)^2 - k_{zN}^2})}$ are the y direction momentum of the electron-like quasiparticles and the hole-like quasiparticles, respectively. Note that, there are two different modes $k_{yN}^{e1(2)}$ corresponding to a set of constant parameters (k_{xN} , k_{zN} , μ , ε and V_S). Indeed, for a certain energy ε , which lies above or below the nodal-line, there are two allowed bands for the electrons, corresponding respectively to two different modes. The iso-energy surface

of the electron-like quasiparticle gives rise to two concentric Fermi discs. The radii of Fermi discs are given as k_{yN}^{e1} (the small one) and k_{yN}^{e2} (the big one). Meanwhile, the iso-energy surface of the hole-like quasiparticle leads to two concentric radius k_{yN}^{h1} (the small one) and k_{yN}^{h2} (the big one). Therefore, an incident electron-like quasiparticle can be scattered by the superconducting potential into four possible modes (two NR modes $k_{yN}^{e1(2)}$ and two AR modes $k_{yN}^{h1(2)}$), as shown in figure 2. Following a standard procedure [19], the probability current of those reflection modes can be calculated directly. Specially, the modes k_{yN}^{e1} , $-k_{yN}^{e2}$, $-k_{yN}^{h1}$, and k_{yN}^{h2} correspond to the probability current, $j_y > 0$, while the modes $-k_{yN}^{e1}$, k_{yN}^{e2} , k_{yN}^{h1} , and $-k_{yN}^{h2}$ correspond to the probability current, $j_y < 0$. Note that, for an incident electron-like quasiparticle with k_{yN}^{e2} ($-k_{yN}^{e1}$), the reflected hole-like quasiparticle with k_{yN}^{h2} ($-k_{yN}^{h1}$) and $-k_{yN}^{h1}$ (k_{yN}^{h2}) corresponds to the intra-mode RAR and the inter-mode SAR, respectively. To achieve a purely real mode $k_{yN}^{e1(2)}$ of the incident electron-like quasiparticle, we must set $(m - Bk_{xN}^2) \geq \sqrt{(\mu + \varepsilon - V_S)^2 - k_{zN}^2}$. Otherwise, the value of k_{yN}^{e1} is imaginary, and the incident mode corresponds to a disappearing k_{yN}^{e1} .

Similarly, the spinor wavefunctions in *S* lead can be given by

$$\begin{aligned} \Psi_{S1(2)}^{e\pm}(y) &= \begin{pmatrix} 1 & w_e^{1(2)} & \Gamma_{Se} & \frac{B(\Upsilon_{1(2)} - (+)q(k_{yS}^{e1(2)} + V_S + \varepsilon - \mu))}{\Delta X_e(V_S - \mu)} \end{pmatrix} e^{\pm i k_{yS}^{e1(2)} y} \\ \Psi_{S1(2)}^{h\pm}(y) &= \begin{pmatrix} 1 & w_h^{1(2)} & \Gamma_{Sh} & \frac{B(\Upsilon_{1(2)} - (+)q(k_{yS}^{h1(2)} + V_S + \varepsilon - \mu))}{\Delta X_h(V_S - \mu)} \end{pmatrix} e^{\pm i k_{yS}^{h1(2)} y} \end{aligned} \quad (7)$$

where $k_{yS}^{e1(2)} = \sqrt{-k_{xN}^2 + \frac{m}{B} - (+)\frac{\sqrt{-k_{zN}^2 + (\sqrt{(\varepsilon^2 - \Delta^2)} + \sqrt{(V_S - \mu)^2})^2}}{B}}$ and $k_{yS}^{h1(2)} = \sqrt{-k_{xN}^2 + \frac{m}{B} - (+)\frac{\sqrt{-k_{zN}^2 + (\sqrt{(\varepsilon^2 - \Delta^2)} - \sqrt{(V_S - \mu)^2})^2}}{B}}$ are the y direction momentum of the electron-like quasiparticles and the hole-like quasiparticles in *S*. The factors in the wavefunctions are given as, $w_e^{1(2)} = -(+)\frac{B(q + B(V_S + \mu)(k_{yS}^{e1(2)} + V_S - \mu))}{X_e(V_S - \mu)}$, $\Gamma_e = \frac{\varepsilon(V_S - \mu) + \sqrt{(\varepsilon^2 - \Delta^2)(V_S - \mu)^2}}{\Delta(V_S - \mu)}$, $w_h^{1(2)} = -(+)\frac{B(B(V_S + \mu)(k_{yS}^{h1(2)} + V_S - \mu) - q)}{X_e(V_S - \mu)}$, $\Gamma_h = \frac{\varepsilon(V_S - \mu) - \sqrt{(\varepsilon^2 - \Delta^2)(V_S - \mu)^2}}{\Delta(V_S - \mu)}$, $X_e = B^2 \sqrt{-k_{zN}^2 + (\sqrt{(\varepsilon^2 - \Delta^2)} + \sqrt{(V_S - \mu)^2})^2}$, $X_h = B^2 \sqrt{-k_{zN}^2 + (\sqrt{(\varepsilon^2 - \Delta^2)} - \sqrt{(V_S - \mu)^2})^2}$, $\Upsilon_{1(2)} = -(+)B(-\Delta^2 + \Upsilon_{1(2)} = -(+)B(-\Delta^2 + \varepsilon(k_{zN} + V_S + \varepsilon - \mu)(V_S - \mu))$, and $q = B\sqrt{(\varepsilon^2 - \Delta^2)(V_S - \mu)^2}$. Since the momentum components k_{xN} and k_{zN} are conserved, the factor $e^{ik_{xN}x + ik_{zN}z}$ in the wavefunctions in *NM* lead and *S* lead is also omitted for brevity.

For solving the scattering properties in the present *NM/S* (shown as figure 2), we suppose an electron-like quasiparticle with energy ε is incident from the left *NM* lead. Thus the wavefunctions in the different leads are

$$\begin{cases} \Psi_N = \Psi_{N2}^{e+}(\Psi_{N1}^{e-}) + r_1(\bar{r}_1)\Psi_{N1}^{e+} + r_2(\bar{r}_2)\Psi_{N2}^{e-} + r_{A1}(\bar{r}_{A1})\Psi_{N1}^{h-} + r_{A2}(\bar{r}_{A2})\Psi_{N2}^{h+}, & y < 0 \\ \Psi_S = t_{S1}^e(\bar{t}_{S1}^e)\Psi_{S1}^{e+} + t_{S2}^e(\bar{t}_{S2}^e)\Psi_{S2}^{e+} + t_{S1}^h(\bar{t}_{S1}^h)\Psi_{S1}^{h-} + t_{S2}^h(\bar{t}_{S2}^h)\Psi_{S2}^{h-}, & y > 0 \end{cases} \quad (8)$$

where r_1 (\bar{r}_1) and r_2 (\bar{r}_2) are the amplitudes of the NRs in *NM*, respectively, r_{A1} (\bar{r}_{A2}) and r_{A2} (\bar{r}_{A2}) are the amplitudes of the ARs in *NM*, respectively, and t_{S1}^e (\bar{t}_{S1}^e), t_{S2}^e (\bar{t}_{S2}^e), t_{S1}^h (\bar{t}_{S1}^h), and

t_{S2}^h (\bar{t}_{S2}^h) are the amplitudes in S , respectively. Note that, the evanescent wavefunctions of the AR hole and NR electron in NM lead should be taken into account to guarantee the conservation of probabilistic current.

To obtain the amplitudes in equation (8), we require the continuity of the wavefunctions and its y -derivative at the interface by the continuity boundary condition $\Psi_N(0) = \Psi_S(0)$ and $\Psi'_N(0) = \Psi'_S(0)$. By solving the boundary condition, we can obtain the expressions for r_1 (\bar{r}_1), r_2 (\bar{r}_2), r_{A1} (\bar{r}_{A2}) and r_{A2} (\bar{r}_{A2}). By the tedious calculation and deduction, we can obtain those general expressions in a very complicated form. However, in some limit cases, we can achieve some simple expressions.

Specially, specific formulas for the AR and the NR coefficients can be given in the limit $k_{xN} = 0$ and $k_{zN} = 0$, when the incident electron momentum lies in y axis. Note that, in this manner, Hamiltonian H_0 in equation (1) decouples into two copies of a scalar non-relativistic Hamiltonian. Thus a k_{yN}^{e2} mode electron can not be scattered into a k_{yN}^{e1} mode since k_{yN}^{e2} and k_{yN}^{e1} belong to different sectors in H_0 . It means that these two modes decouple with each other. Similarly, for the hole-like quasiparticles with the modes k_{yN}^{h2} and k_{yN}^{h1} , they also decouple with each other. However, the modes k_{yN}^{h2} and k_{yN}^{h1} can be coupled to the modes k_{yN}^{e2} or k_{yN}^{e1} by the superconducting pair potential $\Delta(x)$. That is to say, a k_{yN}^{e2} (k_{yN}^{e1}) mode incident electron can only convert into the two allowed k_{yN}^{h2} or k_{yN}^{h1} mode hole in the Andreev reflection process at the superconducting interface. In fact, at $k_{zN} = 0$, a RAR hole can be only allowed in the same mode as its incident wave mode, so the mode remains unchanged and undisturbed. A SAR hole, in contrast, does allow the mode opposite to its incident wave mode. Note that, the modes k_{yN}^{e2} , k_{yN}^{e1} , k_{yN}^{h2} , and k_{yN}^{h1} would couple with each other by a nonzero k_{zN} . Consequently, the inter-mode scattering processes in the AR and the NR can take place at the present superconducting junction.

Note that we only focus on the $k_{N2}^e = \sqrt{\frac{m+(\varepsilon+\mu)}{B}}$ incident in the limit $k_{xN} = 0$ and $k_{zN} = 0$ at here. By the calculation in Appendix, we first obtain the expressions for the RAR ($\mu > \varepsilon$) and the NR. Specifically, for a $k_{yN}^{e2} = \sqrt{\frac{m+(\varepsilon+\mu)}{B}}$ incident, we can get $r_1 = 0$, $r_{A1} = 0$, $r_{A2} = -\Delta\delta(\eta + \kappa)/(2\Omega\lambda\delta + \varepsilon(\delta + \lambda)(\eta + \kappa) + \Omega(2\eta\kappa - (\lambda - \delta)(\eta - \kappa)))$ and $r_2 = \sqrt{1 - (r_{A2})^2}$, where $\eta = \sqrt{m + |\mu - V_S| - \Omega}$, $\kappa = \sqrt{m + |\mu - V_S| + \Omega}$, $\lambda = \sqrt{m + \varepsilon - \mu}$, $\delta = \sqrt{m + \varepsilon + \mu}$, and $\Omega = \sqrt{\varepsilon^2 - \Delta^2}$. While for a $k_{yN}^{e1} = \sqrt{\frac{m-(\varepsilon+\mu)}{B}}$ incident, the results can be given in a similar manner and in the converse order. As a result, the values of r_2 (r_1) and r_{A2} (r_{A1}) equate to zero for the k_{yN}^{e1} (k_{yN}^{e2}) mode incident, while r_1 (r_2) and r_{A1} (r_{A2}) are allowed as a function of ε , μ , Δ , and V_S . In the limit $\mu = V_S/2$ with $\varepsilon, \Delta \ll m, V_S$, we can obtain that $r_{A2} = -i$ and $r_2 = 0$ for the k_{yN}^{e2} mode incident. Moreover, r_{A2} has a first order pole at $\mu = V_S$. Clearly, the RAR is perfect ($r_{A2} = 1$ and

$r_2 = 0$) at $\mu = V_S/2$ and reaches its singularity (r_{A2} reaches to a minimum value and r_2 inversely) at $\mu = V_S$.

While for the SAR case ($\mu < \varepsilon$), the things become much intriguing. For a $k_{yN}^{e2} = \sqrt{\frac{m+(\varepsilon+\mu)}{B}}$ incident, we can get $r_1 = 0$, $r_{A2} = 0$, $r_{A1} = -\Delta\delta'(\eta' + \kappa')/(m\Omega + \varepsilon(\Omega + \delta'(\eta' + \kappa')) + \Omega\eta'\kappa')$, and $r_2 = \sqrt{1 - (r_{A1})^2}$, where $\eta' = \sqrt{m + V_S - \Omega}$, $\kappa' = \sqrt{m + V_S + \Omega}$, $\delta' = \sqrt{m + \varepsilon}$, and $\Omega = \sqrt{\varepsilon^2 - \Delta^2}$. In the case of $k_{yN}^{e1} = \sqrt{\frac{m-(\varepsilon+\mu)}{B}}$, the results can be given in a converse order similar to the case of the RAR. It is clear to see that the SAR is an inter-mode exchanging process, a k_{yN}^{e1} (k_{yN}^{e2}) mode electron converts into a k_{yN}^{h2} (k_{yN}^{h1}) mode hole. In the limit $\mu = 0$ with $\varepsilon, \Delta \ll m, V_S$, we can obtain that $r_{A1} = -\frac{i2\sqrt{m(m+V_S)}}{2m+V_S}$ and $r_2 = \frac{V_S}{2m+V_S}$ for the k_{yN}^{e2} mode incident. Note that the perfect SAR can be obtained ($r_{A1} = 1$ and $r_2 = 0$) at $V_S = 0$. The results are plotted in figure 3 for the two opposite regimes $\mu > \varepsilon$ and $\mu < \varepsilon$. Physically, the inter-mode exchanging feature can be elucidated by the mode in the normal metal lead. In general, the AR mode is $k_{yN}^{h2,1} = \sqrt{\frac{m \pm (\mu - \varepsilon) \text{sign}(\mu - \varepsilon)}{B}}$. For the RAR, $\mu > \varepsilon$, thus $k_{yN}^{h2} = \sqrt{\frac{m+(\mu-\varepsilon)}{B}}$ and $k_{yN}^{h1} = \sqrt{\frac{m-(\mu-\varepsilon)}{B}}$. On the other hand, $\mu < \varepsilon$, the SAR mode can be given as $k_{yN}^{h1} = \sqrt{\frac{m+(\mu-\varepsilon)}{B}}$ and $k_{yN}^{h2} = \sqrt{\frac{m-(\mu-\varepsilon)}{B}}$. It is clearly shown that the AR hole exhibits an inter-mode exchanging. Therefore, in contrast to the intra-mode RAR, the SAR is an inter-mode scattering process.

In the case where k_{zN} is finite, the AR and the NR coefficients exhibit a richer structure at both those limit cases. We focus again on the case of the incidence of k_{yN}^{e1} and k_{yN}^{e2} modes. The dependence of the AR and the NR coefficients on the Fermi energy and the incident energy can be calculated by using equation (1). Note that Hamiltonian H_0 in equation (1) couples the two modes with each other with a nonzero k_{zN} . Thus those two modes can scatter into each other, no matter which type of quasiparticles, the NR electron and the AR hole. It means that the inter-mode and intra-mode scattering processes in the AR and the NR are allowed at the present case. The results of the calculations are shown in figure 6, where the AR and the NR coefficients are plotted as functions of ε for different parameter values.

By using the reflection amplitudes, the zero temperature differential conductance of the present NM/S heterojunction can also be given by the following formula [36–41, 44],

$$G(\varepsilon) = G_0 \left[\int (1 - |r_1|^2 - |r_2|^2 + |r_{A1}|^2 + |r_{A2}|^2) dk_{xN} dk_{zN} + \int (1 - |\bar{r}_1|^2 - |\bar{r}_2|^2 + |\bar{r}_{A1}|^2 + |\bar{r}_{A2}|^2) dk_{xN} dk_{zN} \right]. \quad (9)$$

Combining equations (8) and (9), the zero temperature tunneling conductance in the present NM/S heterojunction can also be investigated extensively and easily by the numerical calculations.

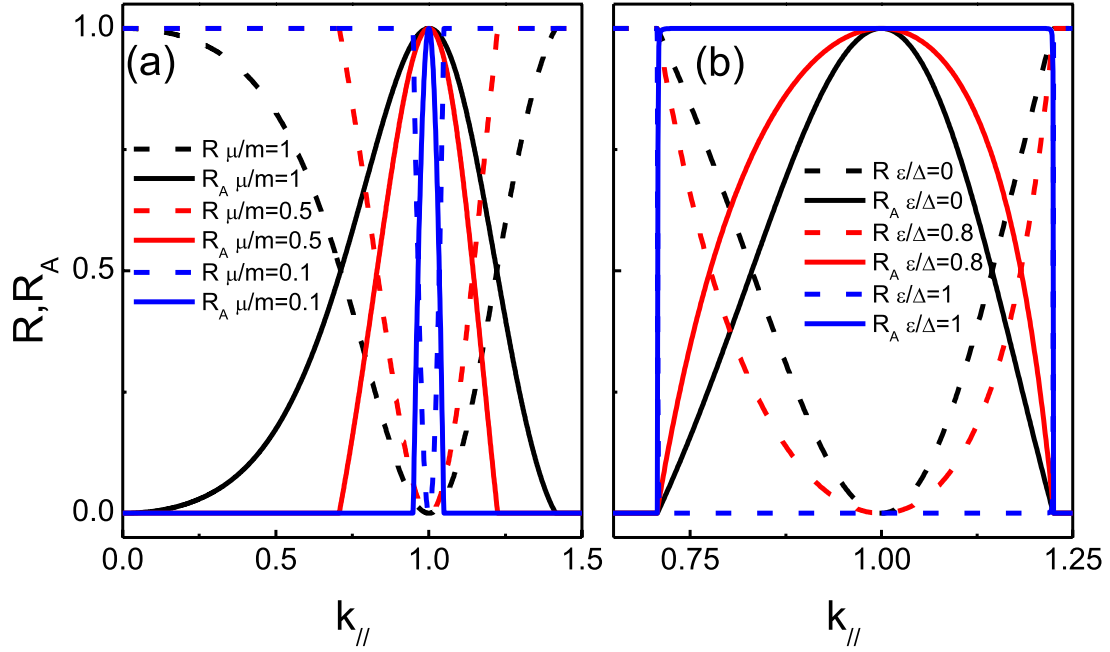


Figure 3. NR and AR coefficients as a function of the transverse momentum $k_{//}$ for different values of Fermi energy μ (a) and incident energy ε (b). In (a) and (b), the constant parameters are $\varepsilon/\Delta = 10^{-2}$ and $\mu/m = 0.5$, respectively. The dashed lines and the solid lines correspond to NR and AR, respectively. The different parameters are shown in the figure.

3. Results and discussion

3.1. Interface parallel to basal plane

We first give the numerical results of the reflection coefficients for the NR electron and the AR hole, as shown in figure 3. The dependence of the reflection coefficients on the transverse momentum $k_{//}$ is calculated by equation (4). The results for several Fermi energies μ are shown in figure 3(a). The same dependence for different incident energies ε is presented in figure 3(b). The parameters used in the calculation throughout the study are $V_S/m = 2.5$, $Bm = 1$, and $\Delta/m = 10^{-3}$.

It is shown that, in contrast to conventional materials and the other topological materials [32, 33, 36–41, 44], the reflection coefficients for the AR hole only have a nonzero value for a special interval of the transverse momentum $k_{//}$. Intuitively, we can get a first glance from figure 1(b) that there is only the special incident angle allowed for impinging on the interface. In fact, the allowed interval for NR can be obtained in $(m - \mu - \varepsilon)/B < (k_{zN}^e)^2 < (m + \mu + \varepsilon)/B$. Since the momentum k_{zN}^e of an incident electron-like quasiparticle is outside the constraint $(m - \mu - \varepsilon)/B < (k_{zN}^e)^2 < (m + \mu + \varepsilon)/B$, the incident wavefunction becomes an evanescent wave, thereby, it can not transmit through the heterojunction, (i.e. it is reflected back completely $r = 1$). Since the difference of the momentum of NR and AR, the allowed interval of the transverse momentum $k_{//}$ is also different. While for AR, the allowed interval for NR can be obtained in $(m - \mu + \varepsilon)/B < (k_{zN}^e)^2 < (m + \mu - \varepsilon)/B$. Beyond this interval, the AR vanishes ($r_A = 0$) and then a total NR ($r = 1$) appears. Clearly, from the constraint, we can see that the allowed interval at a fixed incident energy ε shrinks with the decrease of the Fermi energy μ , as shown in figure 3(a). Note that, the allowed interval shrinks from both

sides to the value $k_{//} = 1$. It is particularly important to point that the allowed interval around $k_{//} = 1$ always survives no matter how small the Fermi energy μ is. Although the general expression is very complicated, we can give some expressions under some special conditions. For $\varepsilon = \Delta$, the amplitude r_A for AR (the electron-like quasiparticle converts into the hole-like quasiparticle) is

$$r_A = \frac{\sqrt{(\mu + \Delta)^2 - (m - Bk_{//}^2)^2}}{2\Delta - \text{sign}(\mu - \varepsilon)\sqrt{(\mu - \Delta)^2 - (m - Bk_{//}^2)^2} + \sqrt{(\mu + \Delta)^2 - (m - Bk_{//}^2)^2}},$$

while the amplitude r for NR (the electron-like quasiparticle reflects back as the electron-like quasiparticle) is

$$r = \frac{\text{sign}(\mu - \varepsilon)\sqrt{(\mu - \Delta)^2 - (m - Bk_{//}^2)^2} + \sqrt{(\mu + \Delta)^2 - (m - Bk_{//}^2)^2} - 2\Delta}{2\Delta - \text{sign}(\mu - \varepsilon)\sqrt{(\mu - \Delta)^2 - (m - Bk_{//}^2)^2} + \sqrt{(\mu + \Delta)^2 - (m - Bk_{//}^2)^2}}.$$

Note that the two regimes of large Fermi energy $\mu > \varepsilon$ and small Fermi energy $\mu < \varepsilon$ correspond to the RAR and the SAR, respectively. At $k_{//} = \sqrt{m/B}$, we readily find $r_A = 1$ for $r = 0$ (no matter the RAR or the SAR), so the conversion between the electron-like quasiparticle and the hole-like quasiparticle occurs with unit probability, as shown in figure 3. This feature is completely different from conventional superconducting heterojunctions, where AR is suppressed if the Fermi wave modes are different across the interface [44]. The perfect AR is a consequence of the Klein-like scattering [30]. Similar phenomenon has also been reported in graphene: the electron-like quasiparticle normally incident on a superconducting interface can convert into the electron-like quasiparticle perfectly without reflection [45].

Another intriguing thing is the perfect AR ($r_A = 1$) at $k_{//} = 1$. This is completely different from that in conversion

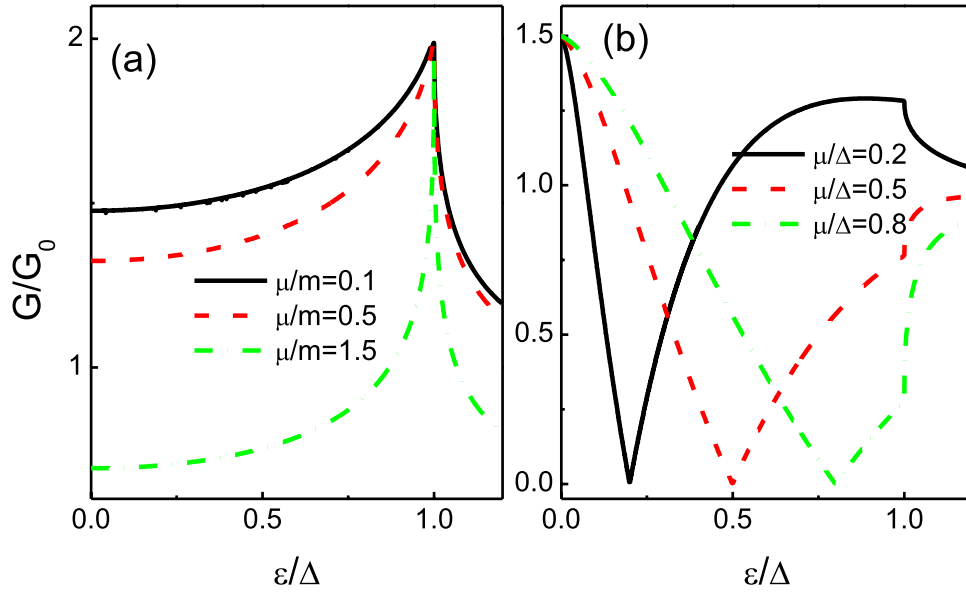


Figure 4. Angularly averaged tunneling conductances for the NM/S heterojunction as a function of the incident energy ε for different values of Fermi energy μ . (a) and (b) denote the cases of $\mu \gg \Delta$ and $\mu < \Delta$, respectively. The Fermi energies are shown in the figure.

materials, where AR is always suppressed at any angle of incidence if the Fermi surface mismatch is present [44]. Meanwhile, the feature is also different from that in graphene and Weyl-point semimetals, where the perfect AR happens only at normal incidence [32, 33, 36–41]. This indicates that the AR in the material can be served as a characteristic feature to detect the unique torus-like energy dispersion. Essentially, the perfect AR has a close relationship with the Klein tunneling effect as stated above.

Similar to figure 3(a), the transverse momentum k_{\perp} dependence of the reflection coefficients for different incident energy ε with $\mu/m = 0.5$ is shown in figure 3(b). It can be seen that the AR coefficients increase with the increase of ε at the allowed interval. For certain parameter value $\varepsilon = \Delta$ the AR is perfect for all allowed angle of incidence. Consequently, it will give a tunneling conductance maximum at $\varepsilon = \Delta$, as is also well known in the existing junctions [31–40]. The novel aspect of the present heterojunction comes from the fact that the regime of the Fermi energy μ is comparable to Δ : $\mu \sim \Delta$. In theory, the width of the allowed interval of transverse momentum k_{\perp} will change with each variety of incident energy ε . In general, the change is not significant when the value of the Fermi energy μ is large. However, at the special case of $\mu = \varepsilon$, the allowed interval shuts down which means that there is no mode allowed. Thus there is no AR for the special case of $\mu = \varepsilon$ and the tunneling conductance vanishes identically. Therefore, for $\mu > \varepsilon$, the allowed interval increases with the increase of ε , while the situation is on the contrary for $\mu < \varepsilon$. In particular, in contrast to conventional RAR in $\mu > \varepsilon$, the AR in $\mu < \varepsilon$ is SAR as reported earlier in [36, 39, 40].

The property of the reflection coefficients directly leads to the fact that angularly averaged tunneling conductances are related to the structure parameters of the NM/S heterojunction. Thereby, the subgap incident energy and the Fermi energy play an important role in the subgap angularly

averaged tunneling conductances. In figures 4(a) and (b), we plot the angularly averaged conductances of the NM/S heterojunction as a function of the subgap incident energy with large Fermi energy $\mu \gg \Delta$ and small Fermi energy $\mu < \Delta$, respectively. Solid lines, dashed lines, and dashed-dotted lines correspond to the cases with various Fermi energies of the heterojunction. From figure 4, we can find three noteworthy features. First, the subgap tunneling conductance for the large Fermi energy decreases with the decrease of the Fermi energy, as shown in figure 4(a). The tunneling conductance reaches a maximum value $2G_0$ at the gap edge $\varepsilon = \Delta$, which is similar to the usual case of a NM/S heterojunction (It has a singularity at $\varepsilon = \Delta$ independent of Fermi surface mismatch.) [32–34, 36, 37, 44]. Second, the subgap tunneling conductance for a small Fermi energy vanishes at $\varepsilon = \mu$, as similar as the case in the graphene NM/S heterojunction [36]. Below the singularity $\varepsilon < \mu$, the subgap tunneling conductance stems from the RAR. While above the singularity $\varepsilon > \mu$, the subgap tunneling conductance mainly comes from the SAR. Therefore, the characteristic suppression of the subgap tunneling conductance curves in figure 4(b) can be regarded as a unique observable signature for the transition from the intra-band RAR to the inter-band SAR. Third, the zero bias tunneling conductance decreases with the increase of Fermi energy. In the limit $E_F \rightarrow 0$, one has $G/G_0 \rightarrow 3/2$. It is sharply different from the case of a graphene NM/S heterojunction where the zero bias tunneling conductance is close to $4/3$ independent of the Fermi energy [36]. It is also dissimilar to the case of the Weyl-point semimetal where the zero bias tunneling conductance always equates to 2 [33, 34]. Due to the charge carrier scattering and the strong potential fluctuations in two dimensional graphene [41, 42], it is difficult to experimentally detect the SAR around the charge neutrality point. With the experimental technology advancement in three dimensional nodal-line Weyl semimetals, it maybe gives a new route to detect the SAR in the coming years.

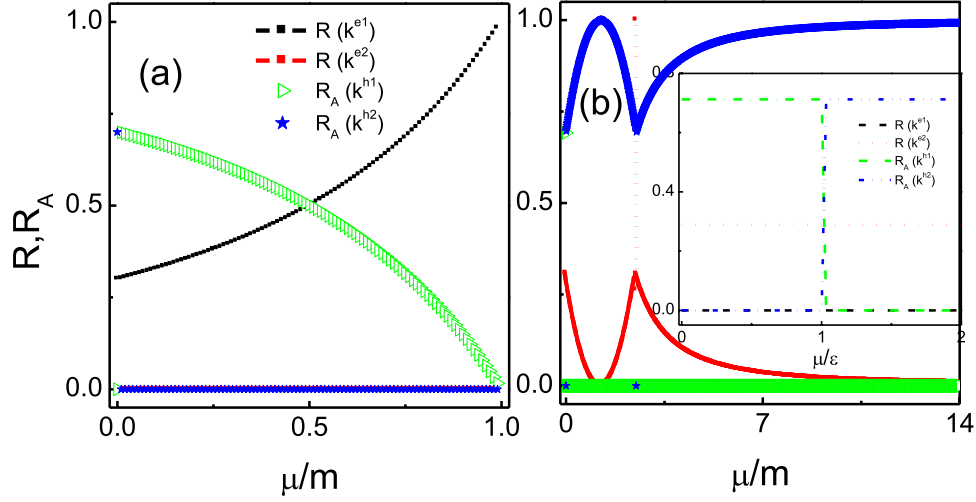


Figure 5. NR and AR coefficients for the present *NM/S* heterojunction as a function of the Fermi energy μ with $k_{xN} = 0$ and $k_{zN} = 0$. (a) and (b) denote the reflection coefficients for an incident electron with $-k_{yN}^{e,1}$ and $k_{yN}^{e,2}$, respectively. The NR and AR coefficients are marked in the figure.

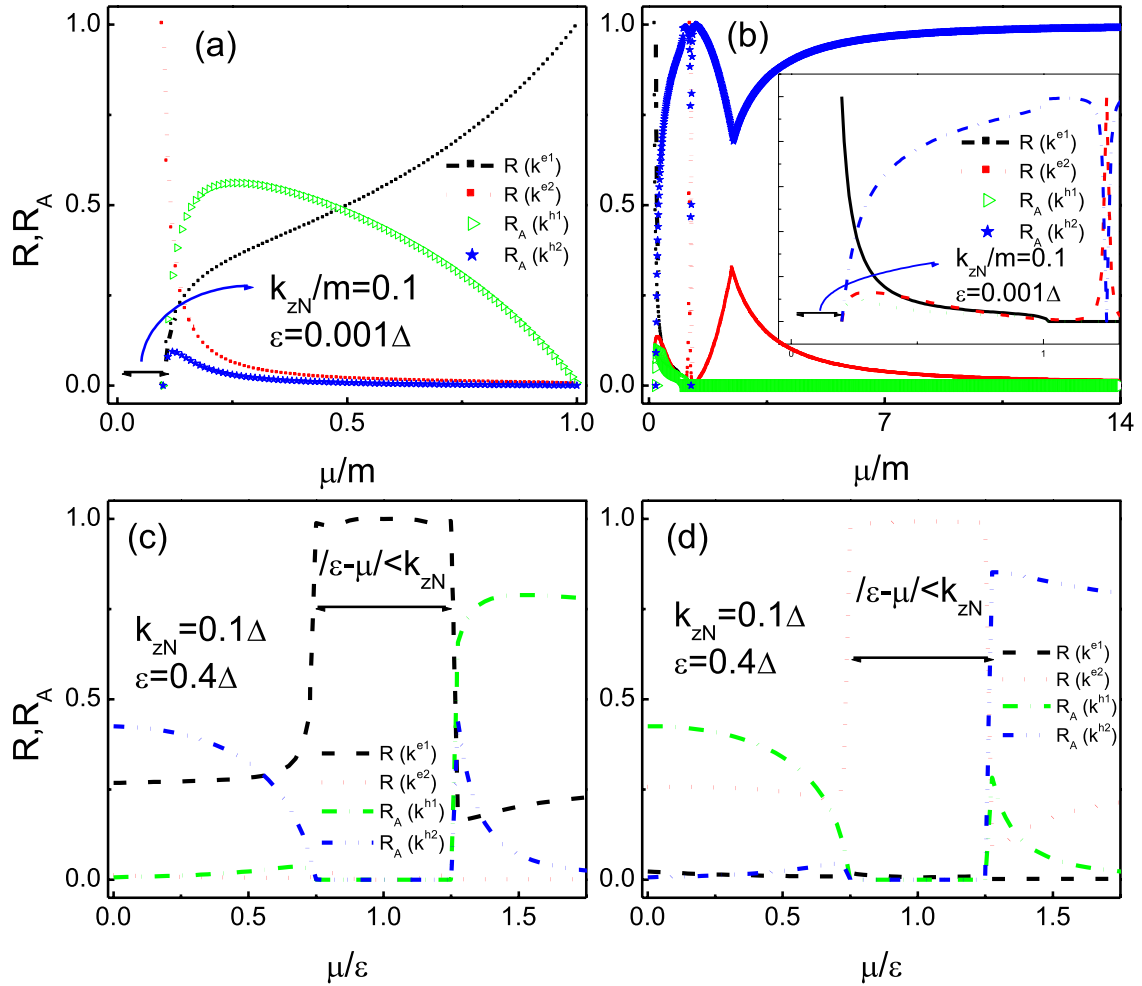


Figure 6. NR and AR coefficients for the present *NM/S* heterojunction as a function of the Fermi energy μ with $k_{xN} = 0$ and $k_{zN} \neq 0$. (a) and (b) Denote the reflection coefficients with a large k_{zN} for an incident electron with $-k_{yN}^{e,1}$ and $k_{yN}^{e,2}$, respectively. (c) and (d) Denote the reflection coefficients with a small k_{zN} for the modes $-k_{yN}^{e,1}$ and $k_{yN}^{e,2}$, respectively. The NR and AR coefficients are marked in the figure.

3.2. Interface perpendicular to basal plane

In contrast to the case parallel to the basal plane (transport along the z axis), an incident electron (transporting along the y axis) can be scattered by the superconducting interface (perpendicular to the basal plane) into four allowed modes, such as, $k_{yN}^{e,1}$, $k_{yN}^{e,2}$, $k_{yN}^{h,2}$, and $k_{yN}^{h,1}$, as shown in figure 2(a). Figures 5 and 6 show the reflection coefficients for the nodal-line Weyl semimetal based NM/S superconducting heterojunction with the interface perpendicular to the basal plane. Note that, non-zero k_{xN} can be regarded as the renormalization of parameter m . Therefore, only the case in the limit $k_{xN} = 0$ will be discussed in this study. First, the AR and the NR coefficients are given in the limit $k_{xN} = 0$ and $k_{zN} = 0$ in figure 5. It is evident that, the inter-mode NR of $k_{yN}^{e,2}$ always equates to zero for the $k_{yN}^{e,1}$ mode incident case, as shown in figure 5(a). When the Fermi energy μ is beyond m , the quantities $k_{yN}^{e,1}$ become imaginary. Consequently, all four scattering modes shut down. Below the critical value $\mu/m = 1$, the scattering of the incident wave with $k_{yN}^{e,1}$ to the intra-mode NR wave with $k_{yN}^{e,1}$, the intra-mode RAR wave $k_{yN}^{h,2}$, and the inter-mode SAR wave $k_{yN}^{h,1}$ may be significant. For $\mu < \varepsilon$, the conversion from the incident electron-like quasiparticle into the hole-like quasiparticle is purely by the inter-mode SAR with $k_{yN}^{h,1}$. Nevertheless, for $k_{yN}^{h,2}$, it only comes from the intra-mode RAR. This feature is similar to type-II Weyl semimetal, but the perfect AR process at the normal incident [33, 34]. As the Fermi energy μ increases, the intra-mode RAR falls down and the intra-mode NR goes up. At allowed interval edge $\mu/m = 1$, they reaches zero and one, respectively.

In figure 5(b), we plot the results for the $k_{yN}^{e,2}$ mode incident case. Essentially, with the increase of the Fermi energy, both the intra-mode RAR with $k_{yN}^{h,2}$ and the inter-mode SAR with $k_{yN}^{h,1}$ all occur. To see it more clearly, we plot the NR and the AR coefficients as a function of ratio μ/ε , as shown in the inset of figure 5(b). It clearly reveals the evolution of inter-mode and intra-mode AR scattering processes. Except the similarities as the results in figure 5(a), they also exhibit some remarkable different features. First, unlike the incident mode $k_{yN}^{e,1}$, the incident mode $k_{yN}^{e,2}$ has no confinement on the Fermi energy. Second, the intra-mode RAR gets a great suppression at $\mu = V_S$, i.e. $R_2 = |r_2|^2 = 1$ and $R_{A2} = |r_{A2}|^2 = 0$. The reduced Hamiltonian with $k_{xN} = 0$ and $k_{zN} = 0$, is essentially the one studied in [32] without a Zeeman field and a pseudoscalar pair potential. This elucidates why the chirality blockade is exhibited in the limit case in a nodal-line Weyl semimetal. Therefore, it can be found that the intra-mode RAR exhibits a reentrant feature with the Fermi energy. However, it gives a perfect asymptotic scattering value $R_{A2} = |r_{A2}|^2 = 1$ as a function of the Fermi energy. Those results indicate that the inter-mode and the intra-mode scattering process are essential in SAR and RAR, respectively. Essentially speaking, those scattering processes are novel and purely relative to AR process. Those results are identical to the analytical solution given in the part B of section 2.

For a finite k_{zN} , the NR and AR coefficients as a function of the Fermi energy μ are shown in figure 6. Clearly, due to the coupling of the modes $k_{yN}^{e,2}$, $k_{yN}^{e,1}$, $k_{yN}^{h,2}$, and $k_{yN}^{h,1}$ by a nonzero k_{zN} , all modes scattering processes (the inter-mode and the intra-mode) in AR and NR can take place. We first focus on the large k_{zN} case. In the high Fermi energy regime, the results exhibit few changes. While in the low Fermi energy regime, the results change a lot. First, there is a scattering gap $\delta\mu = k_{zN}$ for both incident modes ($k_{yN}^{e,2}$ and $k_{yN}^{e,1}$). To see this effect more clearly, we give an enlarged figure in figure 6(b). Second, under this regime, the inter-mode NR scattering becomes significant, which is similar to the case of a potential barrier [44]. It rules out of the intra-mode NR scattering, if $\mu + \varepsilon$ is close to k_{zN} : in this limit $R_2 = |r_2|^2 = 1$ for $k_{yN}^{e,1}$ and $R_1 = |r_1|^2 = 1$ for $k_{yN}^{e,2}$ when $\mu + \varepsilon \rightarrow k_{zN}$, as shown in figures 6(a) and (b). Furthermore, note that, unlike the $k_{zN} = 0$ case, the intra-mode AR scattering process for the $k_{yN}^{e,2}$ incident mode gives rise to a sharp dip structure and completely shuts down at $\mu = V_S/2 - k_{zN}$. While the perfect intra-mode NR scattering process at $\mu = V_S$ in the limit $k_{zN} = 0$ case has been removed by the finite k_{zN} . In fact, the pole of the reentrant structure also exhibits an energy shift (about k_{zN}) to the lower energy direction.

Next we turn to the small k_{zN} case. Figures 6(c) and (d) are, in some respects, similar to the case of $k_{zN} = 0$, such as, the inter-mode SAR dominating for $\mu < \varepsilon$ and the intra-mode RAR dominating for $\mu > \varepsilon$ as shown in the inset of figure 5(b). However, there are some important differences. In such a situation a AR gap about $2k_{zN}$ occurs. In the gap, the ARs with the imaginary modes are prohibited and the intra-mode NR scattering process dominates. To fulfill the probability current conservation, there is also a slight inter-mode NR scattering process. Besides, the ARs and NRs coefficients have a notable change with the increase of the Fermi energy μ . Therefore, the novel features will also give definitive signatures for detecting the inter-mode SAR and the intra-mode RAR in the tunneling conductance.

The property of the reflection coefficients directly leads to the fact that the tunneling conductances are closely related to the incident energy ε and the Fermi energy μ . In figures 7(a)–(d) we plot the tunneling conductances of the present NM/S heterojunction as a function of the incident energy ε with different Fermi energy μ . For a large Fermi energy μ , it can be seen that the tunneling conductance of the mode $-k_{yN}^{e,1}$ exhibits a clear nonmonotonic effect with the Fermi energy. The reason is that the allowed the intra-mode NR and the intra-mode RAR show nonmonotonic features with the Fermi energy μ , as shown in figure 6(a). Beyond the limit case $\mu/m = 1$, the incident wave almost vanishes (except some special incident angles) and gives rise to a nearly zero tunneling conductance. While for the mode $k_{yN}^{e,2}$, the tunneling conductance becomes more intriguing. Clearly, the reflection coefficients have two reentrant structures (around $\mu = V_S/2$ and $\mu = V_S$) as a function of the Fermi energy μ . Therefore, the tunneling conductance will exhibit different features as a function of the incident energy ε at different energy intervals. For example, comparing

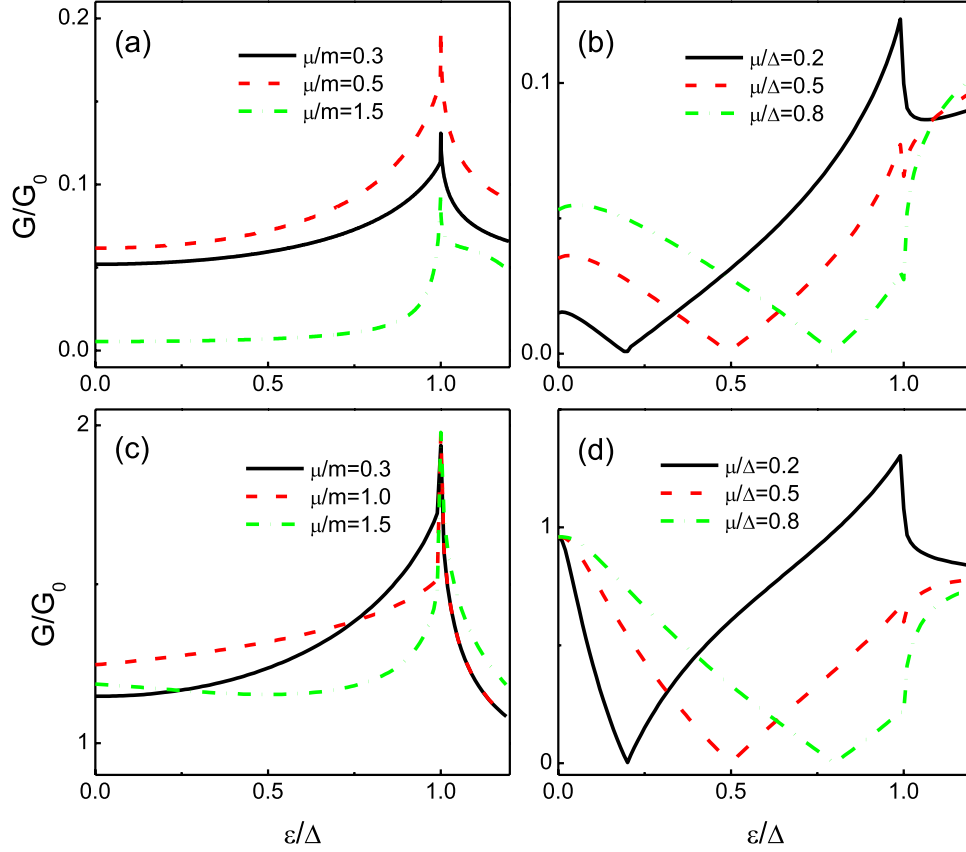


Figure 7. Tunneling conductances of the present *NM/S* heterojunction as a function of the incident energy ε with $k_{xN} = 0$ and $k_{zN} \neq 0$. (a) and (c) Correspond to the tunneling conductances with a large μ for an incident electron with $-k_{yN}^{e,1}$ and $k_{yN}^{e,2}$, respectively. (b) and (d) Denotes the tunneling conductances with a small μ for the mode $-k_{yN}^{e,1}$ and $k_{yN}^{e,2}$, respectively. The different parameters are shown in the figure.

to the case of the mode $-k_{yN}^{e,1}$, the reflection coefficients have a larger change between the case of normal incident and oblique incident. Therefore, the tunneling conductance shows a complex feature in the energy regime $[0, V_S/2]$, as shown in figure 7(c). However, in $[V_S/2, V_S]$, the reflection coefficients all monotonically vary with the Fermi energy (no matter normal incident or oblique incident), as shown in figures 5(b) and 6(b). As a result, the tunneling conductance shows a clear reentrant behavior with the fixed Fermi energy μ in the superconducting gap regime ($\varepsilon < \Delta$). Those features can be understood by the reflection coefficients revealed in figures 5 and 6.

For a small Fermi energy μ , the mode $-k_{yN}^{e,1}$ is comparable to the mode $k_{yN}^{e,2}$. Therefore, the tunneling conductances of the modes $-k_{yN}^{e,1}$ and $k_{yN}^{e,2}$ exhibit the similar features with the different Fermi energies. The results of the modes $-k_{yN}^{e,1}$ and $k_{yN}^{e,2}$ have been given in figures 7(b) and (d), respectively. Similar to the case in graphene and the part A in Sec. III, the tunneling conductances give a clear conversion effect from the SAR to the RAR [36, 45]. Essentially, with the increase of the incident energy ε , the RAR occurs and suppresses. As a result, the tunneling conductance stemming from the RAR can be suppressed by the incident energy ε . The hallmark of the

zero tunneling conductance is a characteristic behavior for the conversion of the RAR and the SAR. When the incident energy ε is bigger than the Fermi energy μ , the tunneling conductance stemming from the SAR grows up again. Overall, by tuning the strength of the incident energy ε , the tunneling conductances with a small Fermi energy μ are dramatically tuned. Therefore it would give an indisputable experimental signature for detecting the SAR. Besides, the zero bias tunneling conductance of $-k_{yN}^{e,1}$ mode has a larger damping slope with the decrease of Fermi energy μ than that of the $k_{yN}^{e,2}$ mode. In the limit $\mu \rightarrow 0$, one has $G/G_0 \rightarrow 0$ and $G/G_0 \rightarrow 1.0$ for the cases of the modes $-k_{yN}^{e,1}$ and $k_{yN}^{e,2}$, respectively. Those are also sharply distinct from the case of the graphene and the other Weyl semimetal *NM/S* heterojunction [33, 34, 36].

4. Conclusions

In summary, we have theoretically investigated the scattering processes of the nodal-line semimetals based *NM/S* superconducting heterojunction based on the BDG equation. For the case of the interface parallel to the basal plane, it is shown that AR is perfect at $k_{\parallel} = \sqrt{m/B}$ due to the Klein-like scattering.

Such perfect AR is different from the case of graphene and Weyl-point semimetals, where it occurs only at the normal incidence. It is also different from the case in the conventional materials, where no perfect AR exists as long as the Fermi surface mismatch is present. While at other incident angle, the AR is suppressed by the Fermi energy μ . However, it is strengthened by the incident energy ε and achieves the perfect AR for all the allowed angles at the superconducting gap edge.

In the case of the interface perpendicular to the basal plane, the pure intra-mode RAR and inter-mode SAR have been revealed at the normal incident. For different incident modes, the reflection coefficients exhibit the different features with the Fermi energy. For one mode, an allowed energy interval exists. Beyond the critical energy, this mode is completely reflected back by the intra-mode NR. While for the other mode, the reflection coefficient exhibits the reentrant behavior with the Fermi energy and saturates at a perfect intra-mode RAR. For an oblique incidence, the reflection coefficient adds another reentrant structure and the whole reentrant structures shift toward the low energy. Basically, those features stem from the torus-like isoenergy surfaces of the nodal-line semimetal, which is in sharp contrast to the case of conventional material, graphene, and Weyl-point semimetals. Those novel scattering processes also give rise to a distinctive tunneling conductance, which can be served as the definitive signature to distinguish the mode-resolved scattering processes in experiments. In particular, a characteristic suppression feature of the tunneling conductance is observed by modulating the incident energy ε with a small Fermi energy μ . Such robust feature can be served as a hallmark for the transition between the RAR

and the SAR. With the advance in experimental technology in the nodal-line semimetal, we thus expect that the revealed features should be observable in the near future.

In addition, we would like to point out that an ideal interface of the superconducting heterojunction is mainly focused in the present study. From the experimental point of view, the interface barrier does exist at the interface. For the case of an interface parallel to the basal plane, the results are slightly affected by the interface barrier because of the Klein tunneling and the magic angles tunneling. When the interface is perpendicular to the basal plane, the Klein tunneling is forbidden [30]. It thus is very amusing to extend the present ideal interface to the real interface cases where an interface barrier is formed. A study in this direction is now in progress.

Acknowledgments

This work was supported by the National Natural Science Foundation of China (Grant No. 11504005, 61675175, and 11874317). CB also acknowledges partial support by Nanhu Scholars Program for Young Scholars of XYNU.

Appendix. The amplitudes for perpendicular case at the limit case

Solving equation (1) in the limit $k_x = 0$ and $k_z = 0$, we can obtain the wavefunctions in the normal lead and superconducting lead as following,

$$\begin{aligned} \Psi_N^{e-}(y) &= \begin{pmatrix} 1 \\ 1 \\ 0 \\ 0 \end{pmatrix} e^{\pm i k_y^e y}, & \Psi_N^{e+}(y) &= \begin{pmatrix} 1 \\ -1 \\ 0 \\ 0 \end{pmatrix} e^{\pm i k_y^e y}, & \Psi_N^{h-}(y) &= \begin{pmatrix} 0 \\ 0 \\ 1 \\ 1 \end{pmatrix} e^{\pm i k_y^h y}, & \Psi_N^{h+}(y) &= \begin{pmatrix} 0 \\ 0 \\ 1 \\ -1 \end{pmatrix} e^{\pm i k_y^h y}, \\ \Psi_S^{e-}(y) &= \begin{pmatrix} 1 \\ 1 \\ \frac{\varepsilon - \sqrt{\varepsilon^2 - \Delta^2}}{\Delta} \\ \frac{\varepsilon - \sqrt{\varepsilon^2 - \Delta^2}}{\Delta} \end{pmatrix} e^{\pm i k_{sy}^e y}, & \Psi_S^{e+}(y) &= \begin{pmatrix} 1 \\ -1 \\ \frac{\varepsilon - \sqrt{\varepsilon^2 - \Delta^2}}{\Delta} \\ -\frac{\varepsilon - \sqrt{\varepsilon^2 - \Delta^2}}{\Delta} \end{pmatrix} e^{\pm i k_{sy}^e y}, \\ \Psi_S^{h-}(y) &= \begin{pmatrix} 1 \\ 1 \\ \frac{\varepsilon + \sqrt{\varepsilon^2 - \Delta^2}}{\Delta} \\ \frac{\varepsilon + \sqrt{\varepsilon^2 - \Delta^2}}{\Delta} \end{pmatrix} e^{\pm i k_{sy}^h y}, & \text{and } \Psi_S^{h+}(y) &= \begin{pmatrix} 1 \\ -1 \\ \frac{\varepsilon + \sqrt{\varepsilon^2 - \Delta^2}}{\Delta} \\ -\frac{\varepsilon + \sqrt{\varepsilon^2 - \Delta^2}}{\Delta} \end{pmatrix} e^{\pm i k_{sy}^h y}. \end{aligned}$$

In the above wavefunction, the wavevectors can be given as $k_{Ny}^{e\pm} = \sqrt{\frac{m\pm(\varepsilon+\mu)}{B}}$, $k_{Ny}^{h\pm} = \sqrt{\frac{m\pm(\mu-\varepsilon)\text{sign}(\mu-\varepsilon)}{B}}$, $k_{Sy}^{e\pm} = \sqrt{\frac{m\pm(\sqrt{\varepsilon^2-\Delta^2}+|\mu-V_S|)}{B}}$, and $k_{Sy}^{h\pm} = \sqrt{\frac{m\pm(|\mu-V_S|-\sqrt{\varepsilon^2-\Delta^2})}{B}}$.

Similar to the above boundary conditions in the text, we match the wavefunctions and its y -derivative at $y = 0$, i.e. $\Psi_L(0) = \Psi_R(0)$ and $\Psi'_L(0) = \Psi'_R(0)$. Solving the boundary conditions one obtains the expression for the AR of a $k_{Ny}^{e+} = \sqrt{\frac{m+(\varepsilon+\mu)}{B}}$ incident.

For the RAR case ($\mu > \varepsilon$), we can get $r^- = 0$, $r_A^- = 0$, $r_A^+ = -\Delta\delta(\eta + \kappa)/(2\Omega\lambda\delta + \varepsilon(\delta + \lambda)(\eta + \kappa) + \Omega(2\eta\kappa - (\lambda - \delta)(\eta - \kappa)))$, and $r^+ = \sqrt{1 - (r_A^+)^2}$, where $\eta = \sqrt{m + |\mu - V_S| - \Omega}$, $\kappa = \sqrt{m + |\mu - V_S| + \Omega}$, $\lambda = \sqrt{m + \varepsilon - \mu}$, $\delta = \sqrt{m + \varepsilon + \mu}$, and $\Omega = \sqrt{\varepsilon^2 - \Delta^2}$.

For the SAR case ($\mu < \varepsilon$), we can get $r^- = 0$, $r_A^+ = 0$, $r_A^- = -\Delta\delta'(\eta' + \kappa')/(m\Omega + \varepsilon(\Omega + \delta'(\eta' + \kappa')) + \Omega\eta'\kappa')$, and $r^+ = \sqrt{1 - (r_A^-)^2}$, where $\eta' = \sqrt{m + V_S - \Omega}$, $\kappa' = \sqrt{m + V_S + \Omega}$, $\delta' = \sqrt{m + \varepsilon}$, and $\Omega = \sqrt{\varepsilon^2 - \Delta^2}$.

ORCID iDs

Chunxu Bai  <https://orcid.org/0000-0002-2921-8869>

References

- [1] Kane C L and Mele E J 2005 *Phys. Rev. Lett.* **95** 146802
- [2] Bernevig B A, Hughes T L and Zhang S-C 2006 *Science* **314** 1757–61
- [3] Zhang D, Lou W K, Miao M S, Zhang S C and Chang K 2013 *Phys. Rev. Lett.* **111** 156402
- [4] Zhang H, Liu C-X, Qi X-L, Dai X, Fang Z and Zhang S-C 2009 *Nat. Phys.* **5** 438
- [5] Hasan M Z and Kane C L 2010 *Rev. Mod. Phys.* **82** 3045
- [6] Hosur P and Qi X L 2013 *C. R. Phys.* **14** 857–70
- [7] Yan B and Felser C 2017 *Annu. Rev. Condens. Matter Phys.* **8** 337
- [8] Wan X, Turner A M, Vishwanath A and Savrasov S Y 2011 *Phys. Rev. B* **83** 205101
- [9] Huang S-M *et al* 2015 *Nat. Commun.* **6** 7373
- [10] Weng H, Fang C, Fang Z, Bernevig B A and Dai X 2015 *Phys. Rev. X* **5** 011029
- [11] Xu S-Y, Belopolski I, Alidoust N and Neupane M Z 2015 *Science* **349** 613
- [12] Lv B Q *et al* 2015 *Phys. Rev. X* **5** 031013
- [13] Xu S-Y *et al* 2015 *Sci. Adv.* **1** e1501092
- [14] Xu N *et al* 2016 *Nat. Commun.* **7** 11006
- [15] Xu S-Y *et al* 2015 *Nat. Phys.* **11** 748
- [16] Belopolski I *et al* 2016 *Phys. Rev. Lett.* **116** 066802
- [17] Souma S *et al* 2016 *Phys. Rev. B* **93** 165121
- [18] Belopolski I *et al* 2016 *Phys. Rev. B* **94** 085127
- [19] Oliver S M *et al* 2017 *2D Mater.* **4** 045008
- [20] Borisenko S *et al* 2019 *Nat. Commun.* **10** 3424
- [21] Xu G, Weng H M, Wang Z J, Dai X and Fang Z 2011 *Phys. Rev. Lett.* **107** 186806
- [22] Bian G *et al* 2016 *Phys. Rev. B* **93** 121113
- [23] Feng B *et al* 2019 *Phys. Rev. Lett.* **123** 116401
- [24] Fang C, Weng H, Dai X and Fang Z 2016 *Chin. Phys. B* **25** 117106
- [25] Li S, Andreev A V and Spivak B Z 2016 *Phys. Rev. B* **94** 081408
- [26] Yesilyurt C, Tan S G, Liang G and Jalil M B A 2016 *Sci. Rep.* **6** 38862
- [27] Sinha D and Sengupta K 2019 *Phys. Rev. B* **99** 075153
- [28] Bai C, Yang Y and Chang K 2016 *Sci. Rep.* **6** 21283
- [29] Bai C, Yang Y and Wei K-W 2016 *Phys. Lett. A* **380** 764
- [30] Khokhlov D A, Rakhmanov A L and Rozhkov A V 2018 *Phys. Rev. B* **97** 235418
- [31] Chen W, Jiang L, Shen R, Sheng L, Wang B G and Xing D Y 2013 *Europhys. Lett.* **103** 27006
- [32] Bovenzi N, Breitzkreuz M, Baireuther P, O'Brien T E, Tworzydło J, Adagideli I and Beenakker C W J 2017 *Phys. Rev. B* **96** 035437
- [33] Hou Z and Sun Q F 2017 *Phys. Rev. B* **96** 155305
- [34] Li X-S, Zhang S-F, Sun X-R and Gong W-J 2018 *New J. Phys.* **20** 103005
- [35] Andreev A F 1964 *Sov. Phys. JETP* **19** 1228
- [36] Beenakker C W J 2006 *Phys. Rev. Lett.* **97** 067007
- [37] Zhang Q, Fu D, Wang B, Zhang R and Xing D Y 2008 *Phys. Rev. Lett.* **101** 047005
- [38] Cheng S-G, Xing Y, Wang J and Sun Q-F 2009 *Phys. Rev. Lett.* **103** 167003
- [39] Yang Y, Bai C, Xu X and Jiang Y 2017 *Carbon* **122** 150
- [40] Yang Y, Zhao B, Zhang Z, Bai C, Xu X and Jiang Y 2016 *Sci. Rep.* **6** 29279
- [41] Lv B, Zhang C and Ma Z 2012 *Phys. Rev. Lett.* **108** 077002
- [42] Martin J, Akerman N, Ulbricht G, Lohmann T, Smet J H, von Klitzing K and Yacoby A 2008 *Nat. Phys.* **4** 144
- [43] Efetov D K *et al* 2016 *Nat. Phys.* **12** 328
- [44] Blonder G E, Tinkham M and Klapwijk T M 1982 *Phys. Rev. B* **25** 4515
- [45] Bhattacharjee S and Sengupta K 2006 *Phys. Rev. Lett.* **97** 217001